Catalysis Science & Technology

ROYAL SOCIETY OF CHEMISTRY

PAPER

Published on 29 October 2026
Licensed under CC-BY 4.0

Check for updates

Cite this: DOI: 10.1039/d6cy00939e

Mechanistic elucidation of selective catalytic ammonia oxidation over Rh by spatially resolved profiling

Fanggang Zhang,†[ab] Daniel Hodonj,†[b] Jiahui Zhang,[a] Patrick Lott, *[b] Olaf Deutschmann [bc] and Ran Sui *[a]

The use of ammonia as a hydrogen carrier and sustainable fuel necessitates efficient control of ammonia slip. In this study, the selective catalytic oxidation (SCO) of ammonia over a Rh/Al_2O_3-coated honeycomb monolith was investigated using spatially resolved capillary sampling. Dry $NH_3/O_2/N_2$ feeds were examined at equivalence ratios φ = 0.1, 0.5, 1, and 2; an additional NO co-feed experiment was conducted to probe the formation pathway of N_2O. Light-off temperatures increase with decreasing φ, consistent with competitive oxygen adsorption on Rh that inhibits NH_3 activation in excess O_2. Under φ = 1, N_2 was the dominant product across the entire temperature window subject to this study, NO_2 was undetected, and N_2O appeared only at low–intermediate temperatures before vanishing at higher temperatures. The NO co-feed experiment indicates that the coupling of NH_3-derived species with NO contributes significantly to N_2O formation. NO showed a three-stage evolution (increase–decrease–increase), with the mid-temperature decline owing to an internal selective catalytic reduction (i-SCR) pathway. Spatial profiles corroborated this mechanism: NH_3 is first oxidized to NO near the monolith inlet, and the nascent NO is subsequently reduced downstream by residual NH_3 to N_2, thereby continuously removing NO along the catalyst. Under fuel-rich conditions, NH_3 decomposition becomes a significant conversion pathway at elevated temperatures, and N_2 selectivity reaches 100% with negligible NO_x formation above 225 °C. Under lean feeds, excess O_2 suppresses the i-SCR pathway, yielding oxidation-dominated chemistry in which NO accumulates and NO_2 forms at high temperature; the N_2O peak shifts to higher temperatures and overall N_2 selectivity declines. These findings provide a mechanistic basis for operation as well as for the design/optimization of Rh-based NH_3-slip control systems.

Received 9th July 2026,
Accepted 27th October 2026

DOI: 10.1039/d6cy00939e

rsc.li/catalysis

Introduction

Ammonia (NH_3) has recently gained strong attention as a carbon-free energy storage medium and hydrogen carrier for renewable electricity, enabling ammonia-to-power concepts such as direct NH_3-fed solid oxide fuel cells (SOFCs) or NH_3 cracking coupled with proton exchange membrane fuel cells (PEMFCs). A practical consequence is NH_3 slip (trace NH_3 in exhaust gases and purge streams), which is expected to become more prevalent as ammonia-based energy systems scale up. NH_3 slip poses serious risks:[1] gaseous NH_3 is toxic and contributes to secondary particulate matter formation; moreover, even ppm-level NH_3 can degrade electrochemical components such as PEM membranes and electrodes. Therefore, efficient NH_3 slip abatement is both an indispensable unit operation for ammonia-based chemical energy conversion and a promising clean-air technology for emission control.

Several approaches for controlling NH_3 slip are under evaluation, including acid scrubbing, membrane separation, catalytic decomposition, and selective catalytic oxidation (SCO) to N_2 and H_2O. Among them, NH_3-SCO is especially promising because it can effectively remove NH_3 in the range of tens to thousands of ppm and operate in oxidizing environments over a broad temperature window,[2] aligning with conditions in fuel cell tail gases and other NH_3-containing vent streams. In parallel, interest in ammonia combustion is growing, yet practical application is limited by narrow flammability limits, comparably poor ignition performance, and high NO_x/N_2O emissions. Catalysts that drive rapid and selective oxidation of NH_3 to N_2 are therefore critical for cleaner energy systems.[3,4] In NH_3-SCO, the target reaction is eqn (1); however, undesired by-

[a] Center for Combustion Energy, Department of Energy and Power Engineering, Tsinghua University, Beijing 100084, China. E-mail: sui@tsinghua.edu.cn
[b] Institute for Chemical Technology and Polymer Chemistry, Karlsruhe Institute of Technology (KIT), Karlsruhe 76131, Germany. E-mail: patrick.lott@kit.edu
[c] Institute of Catalysis Research and Technology, Karlsruhe Institute of Technology (KIT), Eggenstein-Leopoldshafen 76344, Germany
† These authors contributed equally.

products (NO, NO_2, and N_2O) can form through the side reactions eqn (2)–(4):

$$4NH_3 + 3O_2 \rightarrow 2N_2 + 6H_2O \quad (1)$$

$$4NH_3 + 5O_2 \rightarrow 4NO + 6H_2O \quad (2)$$

$$4NH_3 + 7O_2 \rightarrow 4NO_2 + 6H_2O \quad (3)$$

$$2NH_3 + 2O_2 \rightarrow N_2O + 3H_2O \quad (4)$$

In the NH_3-SCO, noble metal-based catalysts are the primary choice.[5,6] Among them, rhodium (Rh) stands out for combining high activity with superior N_2 selectivity in NH_3 oxidation. While platinum (Pt) often exhibits high activity through the Ostwald pathway,[7] Rh typically yields more N_2 and less NO_x (ref. 8–10) and is also effective for NH_3 cracking.[11] Previous density functional theory (DFT) comparisons of palladium (Pd), Pt, and Rh have shown that a stepped Rh surface is the most N_2-selective, owing to a higher activation barrier of NO from adsorbed N and O relative to those on Pt or Pd.[4] Over supported noble metals, NH_3 oxidation has been proposed to proceed through partial oxidation of NH_3 to adsorbed NO followed by reduction of NO by remaining NH_3.[8] Despite the existing progress, the catalytic mechanisms controlling product selectivity remain insufficiently understood, hindering both the rational design of higher-performance catalysts and the development of NH_3 slip abatement units for ammonia-to-power systems. In particular, the dominant reaction pathway is highly sensitive to temperature and O_2 concentration,[12,13] and the interplay between these variables is still debated. Direct steady-state evidence resolving the axial formation of NO and its subsequent reduction within the catalyst bed remains limited. Moreover, the dependence of this internal oxidation–reduction sequence on equivalence ratio and its contribution to N_2O formation are still not fully clarified. Spatially resolved concentration profiling is therefore well suited to address these mechanistic gaps. In this work, we investigated selective catalytic oxidation of ammonia over Rh/Al_2O_3 using both end-of-pipe and spatially resolved measurements to elucidate pathway control and identify the determinants that govern N_2 selectivity.

Experimental

Catalyst preparation and characterization

The catalyst was prepared as described in our previous work.[14] In brief, Rh was deposited onto γ-Al_2O_3 (Puralox TH 100/150, Sasol) by incipient-wetness impregnation using an aqueous $Rh(NO_3)_3$ precursor solution (Acros Organics). The impregnated powder was then formulated as a water-based slurry with AlO(OH) (Disperal P2, Sasol) at a mass ratio of 9 : 1, acidified with aqueous HNO_3 (Fischer), and applied as a washcoat onto a cordierite honeycomb monolith (length 3 cm, diameter 1.6 cm, 400 cpsi, 97 channels) by dip-coating. The coating procedure was repeated until the target loading of 100 g_{cat} L^{-1} was reached, followed by calcination at 550 °C for 5 h to consolidate the washcoat. The effective washcoat thickness was approximately 33 μm, and the post-coating channel cross-section was approximately 1.1 mm × 1.1 mm. The final Rh loading in the washcoat was determined to be 1.56 wt% by inductively coupled plasma optical emission spectroscopy (ICP-OES). The BET specific surface area of 135 m^2 g^{-1} for Rh/Al_2O_3 was measured by N_2 physisorption at −196 °C. CO chemisorption measurements following the previously described procedure[14,15] yielded a Rh dispersion of 25%. For the temperature-programmed desorption of ammonia (NH_3-TPD), the samples were firstly pretreated at 500 °C for 60 min under N_2 flow with a heating rate of 2 K min^{-1} to remove pre-adsorbed species. After cooling to 100 °C, ammonia adsorption was carried out at 100 °C using a gas mixture of 1000 ppm NH_3 in N_2 at a total flow rate of 1 L min^{-1} until saturation. Physisorbed NH_3 was then removed by purging in N_2 at 100 °C for 60 min, before the sample was heated from 100 to 650 °C at 2 K min^{-1} under 1 L min^{-1} N_2 while quantifying the desorbed NH_3 by FTIR (MKS MultiGas 2030). The NH_3-TPD profile (Fig. S1) shows two desorption peaks centred at ~180 and ~240 °C. The total acidity is 160 μmol g^{-1}, in good agreement with previous work.[16]

Catalyst test bench

The test bench has been detailed elsewhere[14,17] and hence is only briefly outlined here. The gaseous feed comprised 2000 ppm NH_3 with O_2 at 750/1500/3000/15 000 ppm, corresponding to equivalence ratios (defined assuming N_2 and H_2O as the products) φ = 2/1/0.5/0.1, balanced in N_2. Additionally, 1000 ppm NO was co-fed at φ = 0.5 to probe the contribution of NO to N_2O formation. The gas hourly space velocity (GHSV) chosen in this work was 75 000 h^{-1}. Fuel-lean conditions are representative of NH_3 dosing in selective catalytic reduction (SCR) aftertreatment where residual slip is a known penalty, whereas fuel-rich kinetics is relevant to NH_3-fueled power and energy conversion systems, although the mole fractions of both reactants are much higher.

Prior to the light-off experiments, the catalyst was oxidized in 10% O_2 (balance N_2) at 500 °C for 1 h. Three consecutive light-off cycles were then recorded at a heating rate of 3 K min^{-1}. Spatially resolved measurements were subsequently carried out on the same sample directly after the light-off experiments. The inlet gas temperature was controlled by the PID controller of the furnace using a thermocouple positioned 5 mm upstream of the monolith. Along the channel, sampling points were taken at 5 mm intervals. To capture the steep NH_3 concentration gradient at the channel inlet, the first 5 mm of the channel were sampled with a finer resolution of 1–2 mm. After each repositioning of the sampling capillary, the system was allowed to stabilize for 20 min before data were recorded. As shown in Fig. 1, axial concentration profiles were acquired

 This journal is © The Royal Society of Chemistry 2026

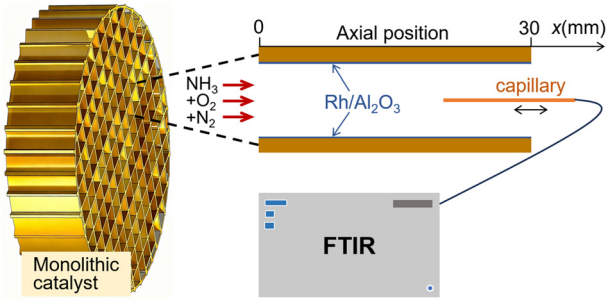


Fig. 1 Schematic of the spatially resolved sampling setup.

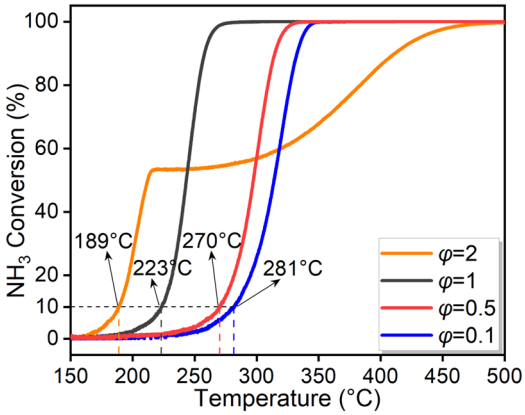


Fig. 2 NH_3 conversion during light-off experiments under different equivalence ratios (φ).

using the Balanced SpaciPro method originally developed by Hlavatý *et al.*[18] and recently implemented in the experimental setup used in our previous study,[19] which yields channel-averaged data by adjusting the suction rate to match residence times in the probed and free channels. The sampling employed a fused-silica capillary (outer diameter: 430 μm; inner diameter: 320 μm; Polymicro), corresponding to ~11% obstruction of the channel's cross-sectional area and a sampling rate of 43% relative to the nominal flow. A previous CFD study[18] has shown that this balanced condition effectively compensates for blockage-induced flow disturbances, allowing the measured axial profiles to represent the undisturbed channel behavior. The sampled stream was diluted 1 : 9 with N_2 and then analyzed online by a Fourier-transform infrared spectroscopy device (FTIR, MultiGas 2030, MKS Instruments). Mole fractions of NH_3, NO, NO_2, and N_2O were quantified directly by the FTIR analyzer; N_2 (IR-inactive) was determined by element balance over all nitrogen-containing species. For the $NH_3/O_2/N_2$ feeds and for the NO co-feed experiment, the nitrogen balances are given by eqn (5) and (6)

$$x_{N_2} = \left(x'_{NH_3} - x_{NH_3} - x_{NO} - x_{NO_2} - 2x_{N_2O}\right)/2 \quad (5)$$

$$x_{N_2} = \left(x'_{NH_3} + x'_{NO} - x_{NH_3} - x_{NO} - x_{NO_2} - 2x_{N_2O}\right)/2 \quad (6)$$

where x' and x denote the inlet and outlet mole fractions, respectively.

Every test was repeated 2–3 times, which yielded excellent repeatability with variations up to ±15 ppm for major species and ±5 ppm for minor species. The determination of experimental reproducibility and uncertainty propagation results can be found in the SI.

Results and discussion

Catalytic activity and product selectivity

Fig. 2 compares the light-off curves of NH_3 oxidation at four representative equivalence ratios (φ = 2, 1, 0.5, and 0.1). Here, T_{10} is defined as the temperature at which NH_3 conversion reaches 10%. The measured T_{10} values are 189 °C (φ = 2), 223 °C (φ = 1), 270 °C (φ = 0.5), and 281 °C (φ = 0.1), respectively. The increase in T_{10} with decreasing φ indicates a monotonic loss of low-temperature activity under progressively more O_2-rich environments. This trend can be explained with a competitive adsorption mechanism: at higher O_2 partial pressures, adsorbed oxygen increasingly occupies active sites and thereby suppresses NH_3 activation. In addition, higher O_2 partial pressure can shift Rh toward a more oxidized state,[20] which further reduces the fraction of metallic Rh sites available for reactant activation[21] and thus also contributes to the delayed light-off. The light-off curve at φ = 2 exhibits a distinct two-stage behavior. At low temperatures, NH_3 conversion proceeds mainly *via* oxidation pathways, although it is limited by the availability of O_2. At higher temperatures above 250 °C, the residual NH_3 is progressively converted through catalytic cracking, in agreement with our recent finding that Rh is active for NH_3 decomposition.[11] The H_2 formation derived from the hydrogen balance (Fig. S4) agrees quantitatively with the NH_3 consumed in this stage, providing direct support for the NH_3 decomposition pathway. Under stoichiometric and lean conditions ($\varphi \leq 1$), the light-off curves exhibit a single continuous rise, consistent with a regime dominated by oxidation, as opposed to a sequential oxidation-cracking process under fuel-rich conditions.

The temperature-dependent mole fractions of the major species at different equivalence ratios are presented in Fig. 3. Under fuel-rich operation (φ = 2), the two-stage NH_3 consumption profile is mirrored by a corresponding two-stage increase in N_2. Neither NO nor NO_2 is detected across the entire examined temperature range. N_2O is the only nitrogen-containing by-product, appearing at low temperatures: its concentration rises to a maximum near 200 °C and vanishes by ~225 °C, indicating that N_2O is an unstable intermediate of NH_3 oxidation that is dissociated at higher temperatures. The disappearance of N_2O at elevated temperatures is not expected to arise from gas-phase decomposition, which generally occurs only at substantially higher temperatures, typically above 800 °C.[22] Thus, the observed N_2O removal is attributed mainly to

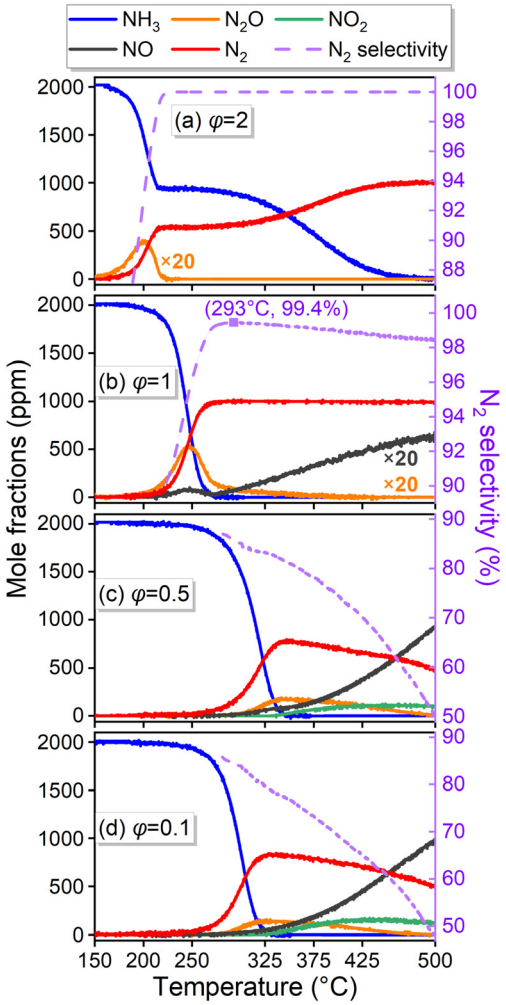


Fig. 3 NH_3 conversion during light-off experiments under different equivalence ratios (φ). Temperature-dependent mole fractions of NH_3, N_2, NO, NO_2, and N_2O, together with N_2 selectivity, at (a) φ = 2, (b) φ = 1, (c) φ = 0.5, and (d) φ = 0.1.

catalytic reactions. In contrast to Pt, on which N_2O tends to desorb,[23] Rh surfaces are known to catalyze the decomposition of N_2O (N_2O + Rh(s) → N_2 + O(s)) even at relatively low temperatures and in the presence of O_2.[24–26] This N_2O decomposition capability is a distinctive advantage of Rh-based catalysts given that N_2O is a greenhouse gas with a 100-year global warming potential (GWP_{100}) 273 times that of CO_2. Furthermore, excess NH_3 can reduce N_2O to N_2, which contributes directly to the superior N_2 selectivity. The pronounced second-stage increase in N_2 at higher temperatures provides strong evidence that NH_3 cracking becomes an increasingly important conversion pathway with rising temperature.

Under stoichiometric conditions, N_2 remains the dominant product. Total NO_x levels remain low and NO_2 is not observed. N_2O again appears only at low–intermediate temperatures, with a peak near ~250 °C, followed by a decline with further heating. This decline reflects the decomposition/reduction of N_2O to N_2. Over the investigated temperature range, NO concentration exhibits a three-stage evolution (increase–decrease–increase). The coincidence of the first NO peak with the N_2O peak suggests that the oxidation routes leading to NO and N_2O will compete in the low-temperature range. The subsequent decline of NO is attributed to an internal selective catalytic reduction (i-SCR) pathway, in which residual NH_3 reduces NO:[27]

$$4NH_3 + 4NO + O_2 \rightarrow 4N_2 + 6H_2O \quad (7)$$

This finding is consistent with the high catalytic activity of Rh for the NH_3 + NO reaction reported by Pérez-Ramírez *et al.*[8] Based on the NH_3-TPD results, the acid sites are expected to retain a reservoir of adsorbed NH_3. These adsorbed species then rapidly consume NO_x intermediates formed on adjacent Rh active sites, shifting the selectivity away from NO and N_2O toward N_2. This is in line with previous findings that higher surface acidity promotes the i-SCR pathway.[28] The i-SCR reaction ceases when NH_3 is fully converted, and then NO rises again. At higher temperatures, N_2O vanishes and NO persists as the sole by-product, at concentrations far below that of N_2.

To identify the surface intermediates that are relevant under the conditions subject to this study and to further elucidate the reaction mechanism, *in situ* DRIFTS measurements were performed. Details of the DRIFTS setup can be found in our recent work.[29] In brief, the spectra were

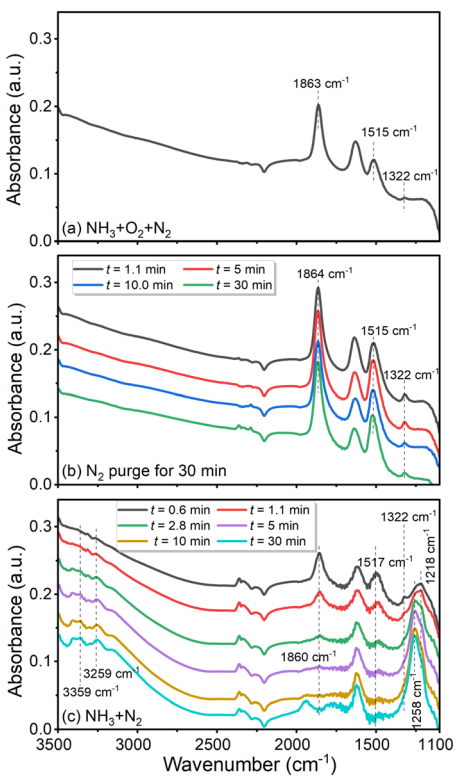


Fig. 4 *In situ* DRIFT spectra at 300 °C: (a) 4000 ppm NH_3 + 3000 ppm O_2 balanced with N_2 until steady state was reached; (b) N_2 purge for 30 min; (c) 4000 ppm NH_3 in N_2.

This journal is © The Royal Society of Chemistry 2026

recorded on a Bruker Invenio S spectrometer equipped with a Harrick cell (BaF_2 windows) and a high-sensitivity MCT detector (800–4000 cm^{-1}, 4 cm^{-1} resolution). Three consecutive steps were then carried out at 300 °C: (a) 4000 ppm NH_3 + 3000 ppm O_2 balanced with N_2 until steady state was reached; (b) N_2 purge for 30 min; and (c) 4000 ppm NH_3 in N_2. It is shown in Fig. 4(a) that a strong band appeared at 1863 cm^{-1}, which is characteristic of nitrosyl species adsorbed on Rh.[30] This species originates from the oxidation of NH_3, providing direct evidence that NH_3 is oxidized to NO(s) on Rh under reaction conditions. The bands at 1515 and 1322 cm^{-1} are assigned to nitro/nitrito species[31] formed by further oxidation of NO(s). When NH_3 and O_2 were switched off and the cell was purged with N_2 (Fig. 4(b)), these bands remained unchanged. This indicates that NO(s) is strongly bound to Rh and hardly desorbs at 300 °C, which is consistent with the results in Fig. 3, where only trace amounts of gas-phase NO were detected below 300 °C. When NH_3 was subsequently introduced (Fig. 4(c)), the Rh–NO band decreased sharply and vanished within approximately 5 min. Its disappearance is attributed to the reaction between NO(s) and NH_3 (or NH_x fragments). The nitro/nitrito species were also progressively removed by NH_3. Meanwhile, new bands developed at 3359/3259 cm^{-1} (antisymmetric and symmetric N–H stretching)[32] and at 1258/1218 cm^{-1} (NH_3 adsorbed on Al_2O_3).[33] NH_3 thus accumulates on the support as the oxidized nitrogen species are consumed. Taken together, these transient DRIFTS experiments resolve the two steps of the i-SCR mechanism: (i) NH_3 is first oxidized by O_2 to NO(s) on Rh, accompanied by nitro/nitrito species formation; and (ii) these oxidized intermediates are then reduced by NH_3.

Under lean conditions, the product distributions at the two O_2 excess levels are qualitatively similar to each other but differ markedly from those observed at φ = 1 and 2. The N_2O peak shifts substantially to higher temperatures, and NO_2 appears, indicating over-oxidation in the presence of excess O_2. In this regard, the calculated NO ⇌ NO_2 equilibrium is compared with the experimental NO_2/NO_x ratios in Fig. S5. Above about 400 °C, the measured ratios coincide with the equilibrium values, indicating that the NO_2 share is governed by thermodynamics at high temperatures. Unlike the stoichiometric case, NO rises monotonically with temperature at an increasingly steep slope, reflecting the strong drive of surplus O_2 toward NO_x formation. Under such oxygen-rich operations, the i-SCR pathway is effectively suppressed because the catalyst surface is dominated by oxygen species rather than NH_x intermediates, resulting in net NO accumulation. As an indirect evidence, 3–5 orders of magnitude higher O(s) and NO(s) coverages over NH_x(s) was recently quantified for a Pt catalyst in our recent work.[3] Meanwhile, N_2 rises rapidly just beyond light-off but then declines gradually as temperature continues to increase. Taken together, these results demonstrate that higher O_2 excess drives nitrogen selectivity away from N_2 and toward NO_x, whereas stoichiometric and fuel-rich operation strongly favor N_2 formation with no detectable NO_2.

N_2 selectivity was evaluated only at $T \geq T_{10}$ for each equivalence ratio to ensure measurable comparisons. Considering carrier N_2 constitutes more than 98% of the stream, changes of the total molar flow between inlet and outlet are marginal and the N_2 selectivity can therefore be expressed as,

$$N_2\ \text{selectivity} = \frac{2x_{N_2}}{x'_{NH_3} - x_{NH_3}} \quad (8)$$

Across the investigated temperature range, the fuel-rich curve consistently exhibits the highest N_2 selectivity: it increases rapidly with temperature and reaches 100% shortly after light-off, remaining essentially at unity up to 500 °C. Two complementary factors account for this trend: firstly, Rh has a lower activation barrier for N_2 formation than for NO formation, as established by DFT;[4] secondly, the O_2-limited environment results in low surface oxygen coverage, which further suppresses the oxidative pathway to NO and kinetically favors N_2 production. At φ = 1, N_2 selectivity increases with temperature to a maximum of 99.4% at ~293 °C, then declines slightly at higher temperatures due to undesirable NO accumulation once NH_3 is depleted and the i-SCR channel ceases. In contrast, N_2 selectivity decreases monotonically with temperature under lean conditions, reflecting a progressive shift toward oxidized nitrogen products (NO and, at high temperature, some NO_2) driven by the excess of surface oxygen.

Spatially resolved profiles

To track species evolution along the catalytic channel, spatially resolved capillary sampling was performed in this work. First, we verified that the products observed within the monolith came predominantly from heterogeneous catalysis rather than from upstream gas-phase reactions. Specifically, the NH_3 mole fractions at the reactor inlet were compared with the capillary-sampled measurements at the monolith entrance (x = 0 mm) at 325 °C and 425 °C. As summarized in Table 1, the relative deviations between the two measurements are less than 2% at all equivalence ratios. Furthermore, the spatially resolved data agree closely with the end-of-pipe data from the light-out experiments (Fig. S6), whereas a deviation is observed with respect to the light-off experiments. This difference can be attributed to the hysteresis between light-off and light-out. We also performed a blank experiment with an uncoated monolith under fuel-lean conditions (φ = 0.1). As shown in Fig. S7,

Table 1 Relative differences between the reactor-entrance and the monolith-entrance NH_3 mole fractions

	φ = 0.1	φ = 0.5	φ = 1	φ = 2
T = 325 °C	0.20%	1.8%	0.84%	0.99%
T = 425 °C	−1.8%	−1.3%	−1.8%	0.10%

the gas-phase contribution was negligible over the entire temperature range. Taking also the small channel height (~1.1 mm) of the coated honeycomb in account, the observed conversions and product distributions can be attributed primarily to catalytic reactions occurring on the Rh/Al_2O_3 washcoat surface.

Fig. 5–7 present the spatially resolved mole-fraction profiles along the monolithic catalyst under different equivalence ratios. Under fuel-rich operation (Fig. 5), neither NO nor NO_2 is detected at any axial position. Since the end-of-pipe results in Fig. 3(a) showed that N_2O reaches its peak concentration near 200 °C, spatial profiles were acquired at this temperature to elucidate where along the channel N_2O is formed and consumed. As shown in Fig. 5(a), N_2O is generated primarily in the upstream region (approximately the first third of the catalytic channel), coincident with the main NH_3 conversion zone. Further downstream, the N_2O mole fraction decreases while N_2 continues to increase, indicating that N_2O is consumed *via* decomposition and reduction to N_2 on Rh. However, at higher temperatures (325 °C and 425 °C, Fig. 5(b) and (c)), no measurable N_2O is detected at any axial position, and N_2 becomes the only nitrogen-containing product. In all cases, the primary consumption zone of NH_3 remains confined to the first third of the monolith; beyond this region, NH_3 conversion proceeds at a markedly lower rate. In the upstream section, NH_3 is rapidly consumed by a faster oxidation reaction as long as O_2 is available; once O_2 is depleted, the residual NH_3 can only be converted through the slower catalytic decomposition, which accounts for the diminished conversion rate in the downstream section.

For the stoichiometric feed (φ = 1), 250 °C was selected because both N_2O and NO exhibit coincident peak

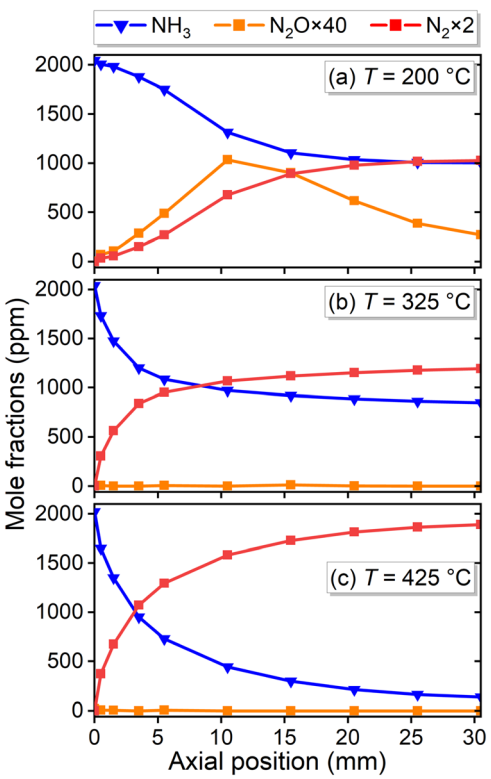


Fig. 5 Spatially resolved mole fraction profiles of NH_3, N_2, NO, NO_2, and N_2O at 200 °C (a), 325 °C (b), and 425 °C (c) under fuel-rich condition (φ = 2).

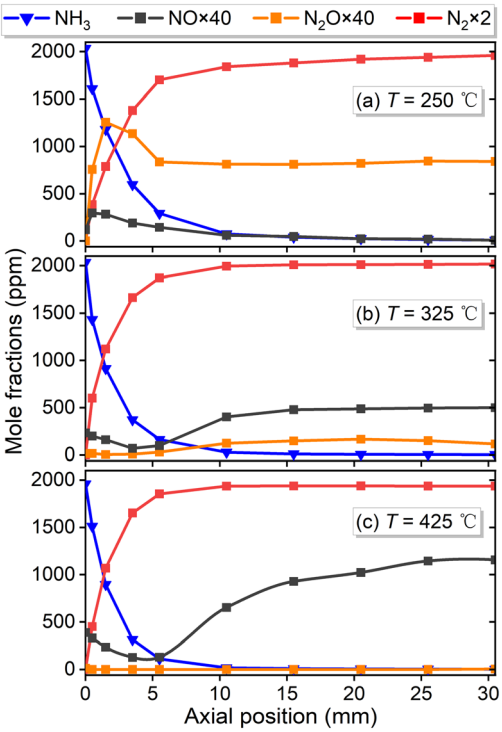


Fig. 6 Spatially resolved mole fraction profiles of NH_3, N_2, NO, NO_2, and N_2O at 250 °C (a), 325 °C (b), and 425 °C (c) under stoichiometric condition (φ = 1).

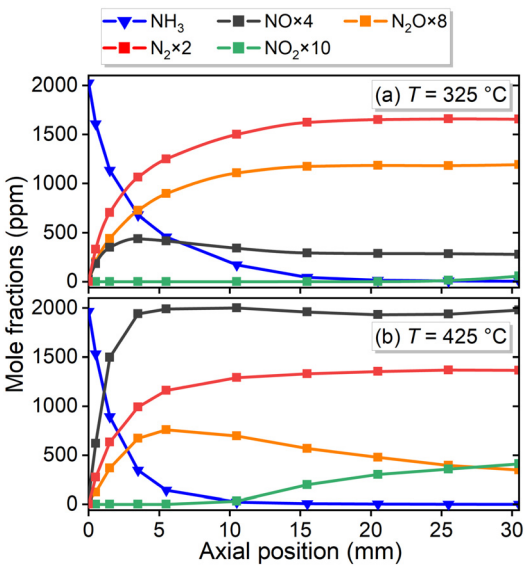


Fig. 7 Spatially resolved mole fraction profiles of NH_3, N_2, NO, NO_2, and N_2O at 325 °C (a) and 425 °C (b) under fuel-lean condition (φ = 0.5).

This journal is © The Royal Society of Chemistry 2026

concentrations near this temperature, as illustrated in Fig. 3(b). At 250 °C (Fig. 6(a)), the mole fractions of both N_2O and NO increase from the monolith entrance, then decrease and finally approach a plateau toward the outlet. The downstream decrease in NO is attributed to consecutive SCR by residual NH_3 to form N_2. NO_2 is not detected at any axial position. The mole fraction of N_2 increases monotonically until the outlet, consistent with its role as the terminal nitrogen product of both the direct selective oxidation and the i-SCR routes. At 325 °C and 425 °C, the axial NO profiles differ markedly from that at 250 °C: NO first decreases, then increases, and finally plateaus toward the catalyst outlet. This trend correlates with variations in the predominant reaction pathway. Near the monolith entrance, the i-SCR pathway consumes NO faster than it is generated, whereas further downstream, as the NH_3 reductant becomes depleted, net NO production resumes and the concentration rises. Consistent with the data shown in Fig. 3, N_2O concentrations at higher temperatures are substantially lower compared to those at 250 °C. Unlike the fuel-rich case, conversion of NH_3 under stoichiometric conditions proceeds predominantly through the oxidation reaction rather than cracking, hence the reaction rate remains high throughout the channel until NH_3 approaches full conversion.

Under lean conditions (φ = 0.5), both N_2 and N_2O increase monotonically with axial position at 325 °C (Fig. 7(a)). By the channel outlet, NH_3 is nearly fully converted, and N_2 is the most abundant product, followed by N_2O. In the downstream section of the monolith, NO is further oxidized into NO_2. At 425 °C, NO_2 formation becomes more pronounced and NO accumulates to substantially higher concentrations, leading to elevated total NO_x and a corresponding decrease in N_2 selectivity relative to the catalyst performance at lower temperatures.

Role of NO in N_2O formation

Based on the discussion above, N_2O is a key intermediate in NH_3-SCO whose formation may proceed *via* two different pathways: (i) oxidation of NH_3 by O_2 alone (eqn (4)), or (ii) oxidation of NH_3 by NO and O_2 jointly (eqn (9)), before NO is further reduced to N_2.[27,34]

$$4NH_3 + 4NO + 3O_2 \rightarrow 4N_2O + 6H_2O \quad (9)$$

To determine the individual relevance of these two reaction pathways to the overall catalyst performance, an additional experiment was performed by co-feeding 1000 ppm NO with both 2000 ppm NH_3 and 3000 ppm O_2. Fig. 8 compares gas-phase species evolution during a light-off under this condition and the baseline case without NO addition. Compared with the baseline experiment, the reaction rate of ammonia decreases slightly at low temperatures when adding NO, suggesting that adsorbed NO competes with NH_3 for active sites and thereby inhibits NH_3 activation. Nevertheless, the desorption of NO is facilitated at higher temperature and releases more surface sites; consequently, the inhibition is relieved. At the same time, surface O atoms from dissociated NO and surface NO itself serve as additional oxidants, accelerating the overall NH_3 conversion rate. Accordingly, mole fractions of N_2O and NO_2 increase relative to the baseline case, owing to the additional oxygen and nitrogen from NO dissociation. The peak N_2O concentration rises from 140 ppm to 585 ppm, which is a more than four-fold enhancement that confirms a direct involvement of NO in N_2O formation. More specifically, this substantial increase indicates that the coupling of surface N/NH_x (dehydrogenation product of NH_3) with adsorbed NO (eqn (9)) is a major route to N_2O. Additionally, a minor contribution from catalytic NO dissociation followed by recombination of adsorbed N with a gaseous NO molecule ($N(s) + NO \rightarrow N_2O$) may also happen, which is known to occur on noble metals.[35]

Notably, the co-fed NO was consumed efficiently. At 305 °C, the net NO conversion reaches 88%, confirming the high SCR activity of Rh. Accounting for the ~26 ppm NO formed concurrently from NH_3 oxidation (Fig. 8, dashed line) this value raises to ~90%. However, a substantial fraction of the consumed NO leads to the formation of N_2O, resulting in a decrease in N_2 selectivity relative to the baseline case at φ = 0.5. Since NH_3 is fully consumed at elevated temperatures and is no longer available to reduce NO, the mole fraction of NO increases steeply. NO detected end-of-pipe therefore comprised both unreacted co-fed NO and additional NO produced from NH_3 oxidation (eqn (2)). Since the *in situ* DRIFTS results show that at 300 °C NO adsorbed on Rh (Rh–NO) hardly desorbs during purging with N_2 (Fig. 4), a higher NO(s) coverage is expected under NO co-feed. Co-fed NO may also compete with NH_3 and O_2 for Rh sites[36] and supply O(s) through dissociation.[37] Nevertheless, the fate of co-fed NO is governed by NH_3: NO consumption ceases once NH_3 is fully converted, while NO_2 formation remains minor, suggesting that NO reacts primarily with NH_3-derived surface species rather than being oxidized.

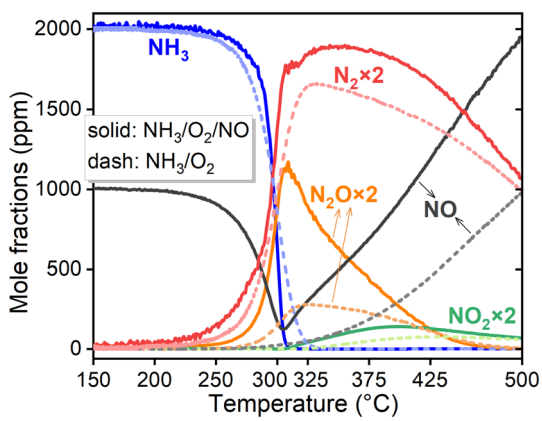


Fig. 8 Temperature-dependent mole fractions of NH_3, N_2, NO, NO_2, and N_2O at φ = 0.5 without (dashed lines) and with (solid lines) 1000 ppm NO co-feed.

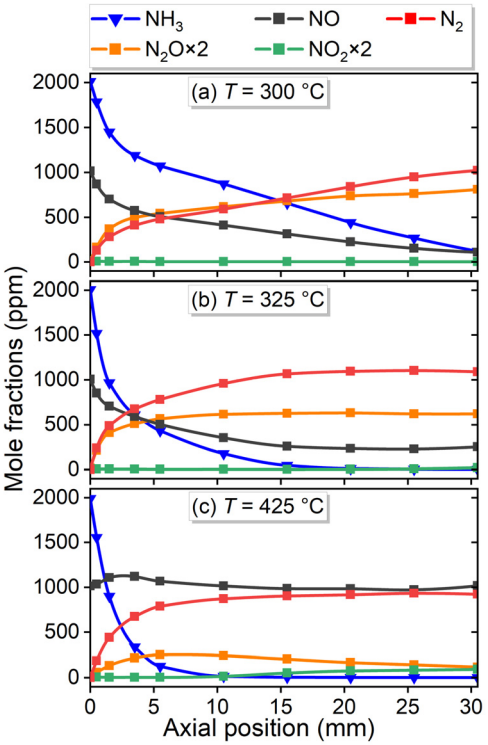


Fig. 9 Spatially resolved mole-fraction profiles of NH_3, N_2, NO, NO_2, and N_2O at 300 °C (a), 325 °C (b), and 425 °C (c) under NO co-feed conditions (2000 ppm NH_3 + 3000 ppm O_2 + 1000 ppm NO).

To further elucidate the evolution of these species along the monolith, spatially resolved profiles were acquired at 300, 325, and 425 °C, as illustrated in Fig. 9. At lower temperatures (300 °C and 325 °C), both NH_3 and NO decrease dramatically in the first third of the catalytic channel. Concurrently, N_2O forms steadily in this region, while N_2 also increases monotonically. The spatial coincidence of NH_3/NO consumption and N_2O formation provides direct evidence that N_2O originates from the reaction between NH_3 and NO (eqn (9)). At 425 °C (Fig. 9(c)), NH_3 is almost completely consumed within the first 5 mm of the monolith because of the fast kinetics at this temperature. N_2O increases only within this narrow region where NH_3 and NO are both abundant. In the NH_3 depletion zone, N_2O is no longer formed and it diminishes downstream by catalytic decomposition. In this downstream region, NO_2 appears by the further oxidation of NO at high temperatures.

Taken together, these data demonstrate that N_2O formation primarily occurs through the reaction between NH_3 and NO. It is worthy to note that under conditions where the i-SCR mechanism takes place, NO generated from NH_3 catalytic oxidation serves a dual role: it is an intermediate that can be consumed *via* SCR to N_2, but it also drives the undesirable side reaction to N_2O. While the i-SCR pathway has been proposed previously for noble-metal catalysts, the spatially resolved profiles provide direct evidence of where NO is formed and where it is subsequently consumed along the channel. Notably, the corresponding reaction zones shift with operating conditions.

Mechanism analysis

With the detailed information obtained from the end-of-pipe and spatially resolved measurements discussed above, a mechanistic picture for ammonia oxidation over Rh is shown in Fig. 10. It should be emphasized that the proposed schematic summarizes the experimentally observed reaction-zone structure along the monolith and is not intended to represent a complete elementary-step surface-reaction network. The overall reaction network comprises several competing pathways, including selective oxidation to N_2 (eqn (1)), partial oxidation to N_2O (eqn (4) and (9)), over-oxidation to NO_x (eqn (2) and (3)), selective catalytic reduction (eqn (7)), and NH_3 decomposition. Their relative contributions to catalyst performance are strongly governed by both temperature and equivalence ratio. Under fuel-rich conditions, the chemistry is dominated by the formation of N_2 with

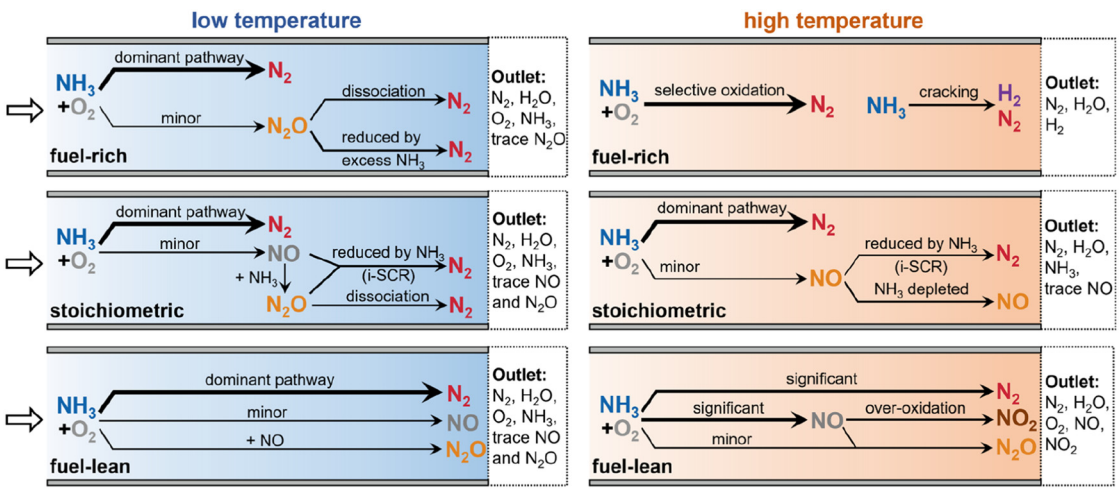


Fig. 10 Proposed reaction pathways for selective catalytic oxidation of NH_3 over Rh/Al_2O_3.

 This journal is © The Royal Society of Chemistry 2026

negligible NO_x evolution above 225 °C. The spatially resolved species concentration profiles reveal that NH_3 is consumed primarily in the upstream section, where O_2 is still available for oxidation. As O_2 becomes depleted further downstream, relatively slower NH_3 conversion continues due to a growing contribution from NH_3 decomposition on Rh. N_2O is observed only in the low-temperature range, where it is formed in the upstream region as an intermediate and is subsequently consumed downstream. Its mitigation at higher temperatures is attributable to two concurrent routes: N_2O catalytic decomposition and selective reduction by excess NH_3. Both pathways drive N_2O toward N_2, leading to the 100% N_2 selectivity from converted NH_3.

Under stoichiometric feed, the reaction mainly proceeds *via* an i-SCR sequence: NH_3 is first oxidized to NO near the monolith inlet before the nascent NO is subsequently reduced downstream by residual NH_3 to N_2 and N_2O.[38,39] N_2O appears at low–intermediate temperatures and then disappears at higher temperatures where it is further converted *via* catalytic decomposition and reduction. The coupled oxidation–reduction pathway removes NO continuously along Rh, accounting for the very high N_2 selectivity (99.4% at approximately 293 °C). However, NO accumulates again in the downstream section at higher temperatures because NH_3 becomes depleted.

Under lean feeds, excess O_2 raises the oxygen coverage, which accelerates NO formation *via* N(s) + O(s) while lowering the NH_x(s) coverage available for NO reduction. The 88% net NO conversion in the NO co-feed experiment at 305 °C under the same lean conditions confirms that the i-SCR pathway remains active (Fig. 8). However, the overall chemistry is oxidation-dominated, with NO accumulating and undergoing further oxidation to NO_2 at elevated temperatures. N_2O remains a transient intermediate, but its concentration peak shifts to higher temperatures relative to the stoichiometric and fuel-rich cases.

Collectively, these findings identify temperature and equivalence ratio as primary levers controlling both activity and N_2 selectivity: catalyst operation under fuel-rich conditions allows to achieve 100% N_2 selectivity and complete NH_3 conversion, whereas increasing temperature and excess O_2 suppress i-SCR and promote NO/NO_2 formation, thereby reducing the N_2 selectivity. Finally, it should be noted that the use of N_2 as the carrier gas in the measurements may shift the chemical equilibrium of N_2-producing reactions; nevertheless, this effect does not alter any of the qualitative findings drawn in this work. In fact, N_2 was deliberately chosen to closely mimic practical application conditions, where exhaust streams are predominantly composed of N_2 rather than inert gases such as Ar or He. The mechanistic insights in this work can provide guidance during the rational design of catalysts and reactors for NH_3-slip abatement and N_2O mitigation applications.

Conclusions

The selective catalytic oxidation of ammonia was investigated over a Rh/Al_2O_3-coated honeycomb monolith using combined end-of pipe, spatially resolved profiling, and *in situ* DRIFTS measurements. The primary findings are as follows:

Light-off temperatures exhibit a monotonic increase with decreasing equivalence ratio, in agreement with a mechanism of competitive oxygen adsorption that inhibits NH_3 activation under conditions of higher O_2 concentration. Within a stoichiometric feed, NH_3 oxidation proceeds *via* an i-SCR mechanism over Rh: NH_3 is first oxidized to NO, and the nascent NO serves as both a product and an intermediate that is subsequently reduced downstream to N_2 by residual NH_3. *In situ* DRIFTS demonstrates that NH_3 oxidation produces Rh–NO(s) together with nitro/nitrito species, which are subsequently consumed by NH_3 exposure. This finding demonstrates Rh′s dual catalytic functionality (oxidation and reduction), which delivers high N_2 selectivity with no detectable NO_2. N_2O appears primarily from the coupling of surface N with NO; it is subsequently removed at higher temperature *via* decomposition or reduction. Under fuel-rich conditions, NH_3 decomposition becomes an increasingly significant conversion pathway at high temperatures once O_2 is consumed, resulting in 100% N_2 selectivity. In lean feeds, however, excess O_2 suppresses the i-SCR route and shifts the NH_3-SCO process toward an oxidation-dominated regime, where NO accumulates and is further oxidized to NO_2.

This work establishes temperature and equivalence ratio as the critical parameters for controlling product selectivity during NH_3 oxidation over Rh catalysts. We show the i-SCR sequence in spatial resolution along the monolith channel and demonstrate the reaction zones shift with operating conditions. These mechanistic insights provide a rational basis for the design and optimization of Rh-based NH_3-slip abatement and N_2O mitigation systems, enabling broader high-selectivity operating windows in ammonia-to-power applications.

Author contributions

Fanggang Zhang: Research design, performed experiments, data analysis, original manuscript. Daniel Hodonj: Performed experiments, data analysis, revised manuscript. Jiahui Zhang: Performed experiments. Patrick Lott: Data analysis, revised manuscript, funding acquisition, project administration. Olaf Deutschmann: Research design, revised manuscript, funding acquisition. Ran Sui: Research design, revised manuscript, funding acquisition, project administration.

Conflicts of interest

There are no conflicts to declare.

Data availability

The data that support the findings of this study are available in KITopen at: https://doi.org/10.35097/c17j9feh8kgzthjn.

Supplementary information (SI) is available. See DOI: https://doi.org/10.1039/d6cy00939e.

Acknowledgements

This work was supported by the National Natural Science Foundation of China (NSFC, Grants 52576126 and 52206157), the Deutsche Forschungsgemeinschaft (DFG, German Research Foundation – SFB 1441 – Project-ID 426888090), and the Dushi Program of Tsinghua University. The authors acknowledge Kathrin Schäfer and Frank M. Bauer, both at ITCP, KIT, for the CO chemisorption measurements and assistance in catalyst preparation, respectively.

References

1 P. Lott and O. Deutschmann, *Proc. Combust. Inst.*, 2023, **39**, 3183–3215.
2 V. Marchuk, D. I. Sharapa, J.-D. Grunwaldt and D. E. Doronkin, *ACS Catal.*, 2024, **14**, 1107–1120.
3 L. Qin, M. Liu, J. Mantzaras, C. K. Law and R. Sui, *Combust. Flame*, 2025, **274**, 113989.
4 H. Ma and W. F. Schneider, *J. Catal.*, 2020, **383**, 322–330.
5 T. Lan, Y. Zhao, J. Deng, J. Zhang, L. Shi and D. Zhang, *Catal. Sci. Technol.*, 2020, **10**, 5792–5810.
6 E. Zhang, F. Zhang, Z. Ren and R. Sui, *Ind. Eng. Chem. Res.*, 2026, **65**, 361–366.
7 V. Marchuk, X. Huang, J.-D. Grunwaldt and D. E. Doronkin, *Catal. Sci. Technol.*, 2023, **13**, 2946–2965.
8 J. Pérez-Ramírez, E. V. Kondratenko, G. Novell-Leruth and J. M. Ricart, *J. Catal.*, 2009, **261**, 217–223.
9 Y. Li and J. N. Armor, *Appl. Catal., B*, 1997, **13**, 131–139.
10 L. Chmielarz, M. Jabłońska, A. Strumiński, Z. Piwowarska, A. Węgrzyn, S. Witkowski and M. Michalik, *Appl. Catal., B*, 2013, **130–131**, 152–162.
11 F. Zhang, H. Wang, E. Zhang, S. Tischer, O. Deutschmann and R. Sui, *J. Phys. Chem. C*, 2025, **129**, 17955–17965.
12 Y. Wang, R. Zhao, K. G. Rappé, Y. Wang, F. Che and F. Gao, *Appl. Catal., B*, 2024, **346**, 123726.
13 H. Liu, Y. Zhao, C. Zhang, Z. Wang, F. Bin, X. Wei and B. Dou, *J. Catal.*, 2023, **425**, 20–31.
14 D. Hodonj, M. Borchers, L. Zeh, G. T. Hoang, S. Tischer, P. Lott and O. Deutschmann, *Appl. Catal., B*, 2024, **345**, 123657.
15 C. Karakaya and O. Deutschmann, *Appl. Catal., A*, 2012, **445–446**, 221–230.
16 P. Osorio-Vargas, C. H. Campos, R. M. Navarro, J. L. G. Fierro and P. Reyes, *J. Mol. Catal. A: Chem.*, 2015, **407**, 169–181.
17 K. Keller, D. Hodonj, L. Zeh, L. Caulfield, E. Sauter, C. Wöll, O. Deutschmann and P. Lott, *Catal. Sci. Technol.*, 2024, **14**, 4142–4153.
18 T. Hlavatý, P. Kočí, M. Isoz, D. Deka and W. Partridge, *Chem. Eng. Sci.*, 2023, **282**, 119272.
19 M. Borchers, D. Hodonj, K. Schäfer, F. M. Bauer and P. Lott, *Catal. Sci. Technol.*, 2026, **16**, 2680–2693.
20 C.-P. Hwang, C.-T. Yeh and Q. Zhu, *Catal. Today*, 1999, **51**, 93–101.
21 A. Takano, S. Tischer, D. Hodonj, P. Lott, O. Deutschmann and J. Kusaka, *Emiss. Control Sci. Technol.*, 2026, **12**, 28.
22 P. Glarborg, J. A. Miller, B. Ruscic and S. J. Klippenstein, *Prog. Energy Combust. Sci.*, 2018, **67**, 31–68.
23 N. R. Avery, *Surf. Sci.*, 1983, **131**, 501–510.
24 J. Oi, A. Obuchi, G. R. Bamwenda, A. Ogata, H. Yagita, S. Kushiyama and K. Mizuno, *Appl. Catal., B*, 1997, **12**, 277–286.
25 K. Doi, Y. Y. Wu, R. Takeda, A. Matsunami, N. Arai, T. Tagawa and S. Goto, *Appl. Catal., B*, 2001, **35**, 43–51.
26 Y. Jing, K. Taketoshi, N. Zhang, C. He, T. Toyao, Z. Maeno, T. Ohori, N. Ishikawa and K.-i. Shimizu, *ACS Catal.*, 2022, **12**, 6325–6333.
27 S. Shrestha, M. P. Harold, K. Kamasamudram and A. Yezerets, *Catal. Today*, 2014, **231**, 105–115.
28 R. Q. Long and R. T. Yang, *J. Catal.*, 2002, **207**, 158–165.
29 F. Zhang, J. Zhang, L. Luo, F. Jacob, S. Tischer, K. H. Luo, O. Deutschmann and R. Sui, *Combust. Flame*, 2026, **289**, 114997.
30 J. Hong, D. Zhang, H. Kwon, C. E. Park, S.-K. Kwon and Y.-H. Kim, *J. Phys. Chem. C*, 2021, **125**, 19733–19755.
31 T. Venkov, K. Hadjiivanov and D. Klissurski, *Phys. Chem. Chem. Phys.*, 2002, **4**, 2443–2448.
32 J. Podobiński and J. Datka, *Molecules*, 2024, **29**, 1726.
33 G. Xu, Y. Zhang, J. Lin, Y. Wang, X. Shi, Y. Yu and H. He, *ACS Catal.*, 2021, **11**, 5506–5516.
34 L. Qin, M. Liu, H. Wang and R. Sui, *Combust. Flame*, 2026, **289**, 115035.
35 E. Fernández, L. Liu, M. Boronat, R. Arenal, P. Concepcion and A. Corma, *ACS Catal.*, 2019, **9**, 11530–11541.
36 T. W. Root, G. B. Fisher and L. D. Schmidt, *J. Chem. Phys.*, 1986, **85**, 4687–4695.
37 T. W. Root, L. D. Schmidt and G. B. Fisher, *Surf. Sci.*, 1983, **134**, 30–45.
38 L. Chen, X. Guan, Z. Fei, H. Asakura, L. Zhang, Z. Wang, X. Su, Z. Yao, L. L. Keenan, S. Hayama, M. A. van Spronsen, B. Karagoz, G. Held, C. S. Allen, D. G. Hopkinson, D. Decarolis, J. Callison, P. J. Dyson and F. R. Wang, *Nat. Commun.*, 2025, **16**, 26.
39 S. Hinokuma, S. Kiritoshi, Y. Kawabata, K. Araki, S. Matsuki, T. Sato and M. Machida, *J. Catal.*, 2018, **361**, 267–277.

 This journal is © The Royal Society of Chemistry 2026